

# YOUNG NEUTRON STARS AND THEIR WIND NEBULAE

Patrick Slane

*Harvard-Smithsonian Center for Astrophysics*

slane@cfa.harvard.edu

**Abstract** With Teragauss magnetic fields, surface gravity sufficiently strong to significantly modify light paths, central densities higher than that of a standard nucleus, and rotation periods of only hundredths of a second, young neutron stars are sites of some of the most extreme physical conditions known in the Universe. They generate magnetic winds with particles that are accelerated to energies in excess of a TeV. These winds form synchrotron-emitting bubbles as the particle stream is eventually decelerated to match the general expansion caused by the explosion that formed the neutron stars. The structure of these pulsar wind nebulae allow us to infer properties of the winds and the pulsating neutron stars themselves. The surfaces of the stars radiate energy from the rapidly cooling interiors where the physical structure is basically unknown because of our imprecise knowledge of the strong interaction at ultrahigh densities. Here I present a summary of recent measurements that allow us to infer the birth properties of neutron stars and to probe the nature of their winds, the physics of their atmospheres, and the structure of their interiors.

**Keywords:** Neutron Star, Pulsar Wind, Cooling, Jets, Filaments

## Introduction

Young neutron stars (NSs) probe some of the most extreme physical environments in the Universe. Their rapid rotations and large magnetic fields combine to accelerate particles to extremely high energies, producing energetic winds that result in the slow spin-down of the stars and generate nebulae of synchrotron-emitting particles spiraling in a wound-up magnetic field. The structure of these nebulae is determined by the energy input from the central pulsars as well as the structure and content of the medium into which they expand. In the centermost regions, relativistic outflows in the form of rings and jets are formed; the geometry of these emission regions reveals the orientation of the pulsar spin axes and can provide information on the formation of kicks imparted in the moments following their formation. Their large-scale struc-

tures reveal details of the magnetic field and signatures of interaction with the ejecta from the explosions that gave them birth.

The stellar interiors are characterized by conditions and physical processes otherwise observed only within the nuclei of atoms. They are born hot, but cool rapidly due to neutrino production in their interiors. However, details of the interior structure of such stars remain poorly understood owing to our incomplete understanding of the strong interaction at ultrahigh densities and, since the neutrino production rate is critically dependent on the structure of the interior, the cooling rate is highly uncertain. In the standard cooling scenario, neutrino production proceeds primarily via the modified Urca process. Residual heat diffuses from the core to the surface, manifesting itself as blackbody-like emission – modified by effects of any residual atmosphere – which peaks in the soft X-ray band. The rate at which the surface temperature declines depends critically upon the neutrino emission rate; thus, its measurement provides constraints on hadronic physics at high densities.

Perhaps the most stunning thing about NSs is the fact that we can actually make measurements that, directly or indirectly, probe the above properties. Particularly with the advent of sensitive high-resolution X-ray observations, we can now image jets and outflows from the wind termination shocks, identify magnetic filaments in the nebular interiors, detect the thermal emission from shock-heated ejecta, and measure directly the pulsations from the rotating stars and the emission from their ultra-hot surfaces. Here I describe the basic properties of young NSs and their nebulae, and summarize recent observational work that has begun a revolution in our understanding of how these stars work. Brevity precludes a thorough review, and the reader is referred to recent articles by Kaspi et al., 2004 and Yakovlev and Pethick, 2004 for additional information and references.

## 1. Pulsar Wind Nebulae

Our basic understanding of PWNe stems from the picture presented by Rees and Gunn, 1974, and expanded upon by Kennel and Coroniti, 1984, in which an energetic axisymmetric wind is injected from a pulsar into its surroundings. As illustrated schematically in Figure 1, the structure of a PWN is regulated by the input power from the pulsar and the density of the medium into which the nebula expands; the pulsar wind and wound-up toroidal magnetic field inflates a bubble which is confined in the outer regions by the expanding shell of ejecta or interstellar material swept up by the SNR blast wave. The boundary condition established by the expansion at the nebula radius  $r_N$  results in the formation of a wind termination shock at which the highly relativistic pulsar wind is decelerated to merge with the particle flow in the nebula. The shock forms at the radius  $r_w$  at which the ram pressure of the wind is balanced by the

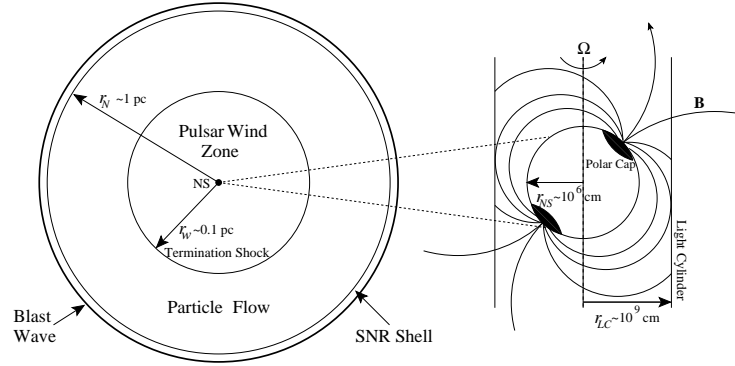


*Figure 1.* Schematic view of a pulsar and its wind nebula. See the text for a complete description. (Note the logarithmic size scaling in the PWN figure when comparing with images shown elsewhere in the text.)

internal pressure of the PWN:

$$r_w = \sqrt{\dot{E}/(4\pi\eta cp)}, \quad (1)$$

where  $\dot{E}$  is the rate at which the pulsar injects energy into the wind,  $\eta$  is the fraction of a spherical surface covered by the wind, and  $p$  is the total pressure outside the shock. Ultimately, the pressure in the nebula is believed to reach the equipartition value; a reasonable pressure estimate can be obtained by integrating the radio spectrum of the nebula, using standard synchrotron emission expressions, and assuming equipartition between particles and the magnetic field. Typical values yield termination shock radii of order 0.1 pc, which yields an angular size of several arcsec at distances of a few kpc.

As the relativistic fluid comprising the PWN encounters the freely-expanding ejecta, Rayleigh-Taylor instabilities result in the formation of a network of dense, optical line-emitting filaments (Jun, 1998). The density and magnetic field strength becomes enhanced in regions where the PWN encounters these filaments, producing enhanced synchrotron emission observed as radio filaments. Due to the pinching effect of the global toroidal magnetic field, the overall morphology of a young PWN is often elongated along the pulsar spin axis (Begelman & Li, 1992; van der Swaluw et al., 2004). Along the rotation axis the flow becomes collimated, producing jets. Pinch instabilities may disrupt the toroidal structure, however, changing the structure of the magnetic field in the outer nebula regions and relaxing the collimation of the jets far from the pulsar (Begelman, 1998).

The overall geometry of the PWN, as well as that of the emission from jets or ring-like structures near the termination shock, thus provides a direct indication of the pulsar geometry. The details of the jet morphology and the emission

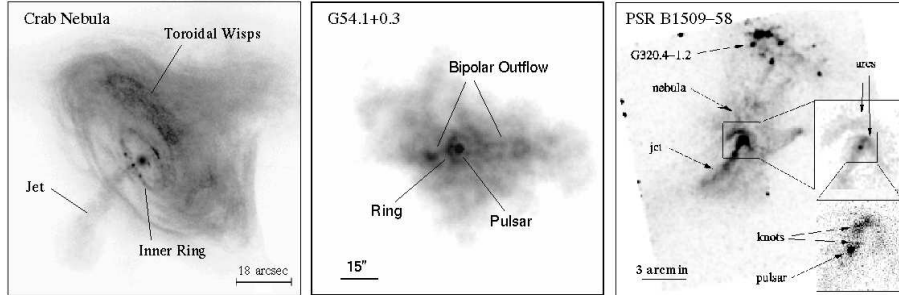


Figure 2. *Chandra* images of the Crab Nebula (left), G54.1+0.3 (center), and PSR B1509–58 (right) showing the complex emission from these PWNe, including jet outflows and toroidal structures.

structure in the postshock region provide the strongest constraints available on wind composition and particle acceleration in PWNe. For cases in which the pulsar proper motion is also known, constraints on the kick velocity mechanism can be derived based on the degree of alignment between the velocity vector and the pulsar spin axis. In later stages the PWN interacts with the reverse shock formed in the SNR in which the NS was born. This interaction causes the disruption of the PWN, often leading to composite SNRs with complicated PWN structures in their interiors.

## 1.1 Jets and Tori

In the inner portions of the Crab Nebula, optical wisps mark the position of the wind termination shock, at a distance of  $\sim 0.1$  pc from the pulsar. The brightness and position of these wisps varies in time, with inferred outflow speeds up to  $0.7c$  (Hester, 1998). As shown in Figure 2 (left), high resolution X-ray images reveal a ring of emission at the position of the wisps (Weisskopf et al., 2000), providing a direct connection between the unshocked pulsar wind and the bulk properties of the nebula. Material from the inner ring forms a series of toroidal X-ray wisps that are variable with time (Hester et al., 2002). The geometry of these X-ray features imply a tilted torus, and a jet of material flows perpendicular to the plane of the toroid, extending some 0.25 pc from the pulsar. A faint counterjet is also observed, along with significantly enhanced X-ray emission from the leading portion of the toroid, presumably the result of Doppler beaming. One troubling aspect of this suggestion is that the brightness distribution around the inner ring does not match that of the outer toroid; indeed, the brightness is rather uniform except for some small clump-like structures that vary in position and brightness with time.

A handful of other PWNe display X-ray features that suggest the presence of extended ring-like structures and narrow collimated components. The size

of the ring-like features places the emission region near the pulsar wind termination shock. The spectral and temporal properties of the collimated structures argue that they are focused jets of high speed material, as observed in the Crab. Such observations have already begun to inspire new axisymmetric MHD models that predict similar features (e.g., Komissarov & Lyubarsky 2004), and ongoing observational studies promise to further constrain and refine such models. In particular, the confining mechanism for jets is not well-understood; many jets display some amount of curvature, with the Vela pulsar jet being an extreme example in which the morphology is observed to change on timescales of months (Pavlov et al., 2003). This may be the result of pinch instabilities disrupting the toroidal structure of the confining magnetic field (Begelman 1998), or could be indicative of an interaction of the jet material with the ambient medium. There also appears to be a wide variation in the fraction of spin-down energy channeled into the jets, ranging from roughly  $2.5 \times 10^{-5}$  for PSR J0205+6449 in 3C 58 to nearly  $10^{-3}$  for PSR B1509–58. And, while Doppler beaming is invoked to explain the large brightness variations in jets and the associated counterjets, as well as around the observed toroidal structures, it is not clear that this alone is sufficient to explain the observations.

*Chandra* observations of G54.1+0.3 (Lu et al., 2002) reveal a central 136 ms pulsar (Camilo et al., 2002a) embedded in a diffuse  $1'5 \times 1'2$  nebula (Figure 2, center). The pulsar is surrounded by an X-ray ring for which the X-ray emission is brightest along the eastern limb. When interpreted as the result of Doppler boosting, this implies a post-shock velocity of  $\sim 0.6c$  (Lu et al. 2002; Romani & Ng 2003). Faint bipolar elongations running roughly east-west, perpendicular to the long axis of the ring, are also observed. These apparent outflows, which presumably lie along the pulsar rotation axis, are more diffuse than the jets in the Crab Nebula, yet appear to carry away a considerably larger fraction of the energy; they comprise roughly the same luminosity as the central ring, which is in stark contrast to the Crab where the torus outshines the jets by a large factor.

*Chandra* observations of PSR B1509–58 (Gaensler et al., 2002) demonstrate that this young and energetic pulsar associated with G320.4–1.2 powers an extended and extremely complicated PWN, with structures on scales from  $\sim 10'$  down to the spatial resolution limit (Figure 2, right). The elongated PWN has a clear axis of symmetry centered on the pulsar, presumably representing the projected orientation of the pulsar spin axis. To the southeast of the pulsar, the nebula is dominated by a narrow jet-like feature approximately 6 pc in length. The lack of a similar feature to the north can be explained by Doppler boosting if the pulsar's spin axis is inclined to the line-of-sight by  $\lesssim 30^\circ$  (Gaensler et al., 2002). In the central regions of the PWN, a pair of semi-circular arcs lie  $\sim 0.5$  and  $\sim 1$  pc to the north of the pulsar. Gaensler et al.

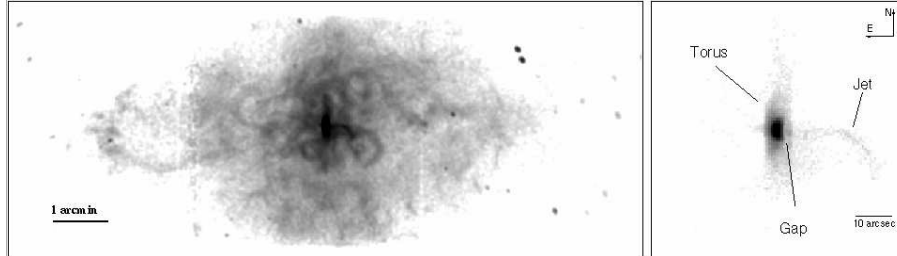


Figure 3. Left: *Chandra* image of 3C 58. Complex filamentary loops fill the interior region. Right: The innermost region of 3C 58 showing the NS embedded in an elongated structure. A curved jet extends to the west, with a hint of a counterjet component in the east.

(2002) note that if the inner region of these arcs represents the position of the pulsar wind termination shock, then the flow time to the arcs is much shorter than the synchrotron lifetime of the emitting particles based on equipartition estimates of the magnetic field. Thus, unlike for the Crab torus, where these timescales are similar, the emission from the arcs is not the result of large synchrotron cooling at this position. Instead, the arcs appear to resemble the series of concentric wisps seen for the Crab which are interpreted as sites of electron compression in an ion-dominated flow (Gallant and Arons, 1994, Gaensler et al., 2002).

The innermost region of 3C 58 (see Figure 3) consists of a bright, elongated compact structure centered on the pulsar J0205+6449. This inner nebulosity is bounded along the western edge by a radio wisp (Frail and Moffett, 1993), and is suggestive of a toroidal structure that is tilted about a north-south axis, with the pulsar at its center. The eastern side of the toroid is slightly brighter than the western side, suggesting that the eastern side is beamed toward us. If interpreted as a circular termination shock zone, the inferred inclination angle in the plane of the sky is roughly 70 degrees (Slane et al., 2002).

The elongated structure extending westward from the position of the pulsar has the appearance of a jet (Figure 3, right). Its orientation is consistent, in projection, with the pulsar rotation axis inferred from the wind termination shock region discussed above, and also the east-west elongation of the entire PWN (Figure 3, left). The structure shows considerable curvature, similar to that seen in the Crab Pulsar jet. A faint structure that may be a counterjet is observed to the east of the pulsar. The observed luminosity is nearly a factor of 10 smaller than that for the torus. For the Crab Nebula, the torus is nearly 20 times more luminous than the jet in X-rays, while for PSR B1509–58 the jet is brighter than the extended inner emission (Gaensler et al. 2002).

The jet/torus morphology observed in these PWNe provides the geometry of the pulsar system, yielding both the projected direction of the spin axis and the

inclination angle. Modeling of such emission in other PWNe holds promise for understanding the kicks that give pulsars their large space velocities (Ng and Romani, 2004). The jets observed in the Crab and Vela pulsars, for example, are aligned with their proper motion vectors (Aschenbach & Brinkman 1975; Helfand et al. 2001). If the kick that gave these pulsars their proper motion was generated in the supernova explosion by some asymmetric mass ejection, then this alignment requires an initial pulsar spin period that is short relative to the kick timescale, so that the impulse of the kick is averaged over many rotations of the star (Lai et al., 2001). Romani and Ng, 2003 reach similar conclusions for PSR J0538+2817 in the supernova remnant (SNR) S147. By modeling the faint extended PWN emission as a jet and torus, they derive a spin axis direction that is aligned with the vector from the SNR center to the current pulsar position. For some pulsars [e.g. J0205+6449 in 3C 58 (Murray et al., 2002) and J1811–1925 in G11.2–0.3 (Kaspi et al., 2001)], we believe that the initial spin period was much longer than typical pulsar kick timescales. This would suggest that their proper motions should not necessarily be aligned with the jet direction. Future radio timing observations of these pulsars will ultimately lead to such proper motion measurements.

## 1.2 Filaments in PWNe

Extensive filamentary structure is observed in  $H\alpha$ , [OIII], and other optical line images of the Crab Nebula. Based on their observed velocities, these filaments form an expanding shell of ejecta that surrounds the nonthermal optical emission from the nebula. High resolution images with HST reveal detailed morphology and ionization structure suggesting that the filaments form from Rayleigh-Taylor instabilities as the expanding relativistic bubble encounters slower moving ejecta (Hester et al., 1996), a picture supported by MHD simulations that show that 60-75% of the swept-up mass ends up concentrated in such filaments (Jun 1998, Bucciantini et al. 2004). Radio observations reveal filaments that coincide with these optical filaments, presumably corresponding to synchrotron emission from regions of enhanced density and magnetic field in the form of magnetic sheaths that form as the pulsar-injected energy encounters the thermal filaments (Reynolds, 1988). Such filamentary structure is not observed in X-rays, however, suggesting that the electrons with sufficient energy to radiate X-rays do not reach the shell of filaments. This is consistent with the observed smaller extent of the X-ray emission in the Crab nebula relative to its radio size, and indicates a larger magnetic field than is observed in 3C 58 and PSR B1509–58.

Recent *Chandra* observations of 3C 58 reveal a complex of loop-like filaments most prominent near the central regions of the PWN (Figure 3, left), but evident throughout the nebula (Slane et al., 2004a). These structures, whose

X-ray spectra are nonthermal, are very well correlated with features observed in the radio band (Reynolds and Aller, 1988). Optical observations reveal faint thermal filaments as well (van den Bergh, 1978), which presumably have an origin similar to that of the Crab filaments. The velocities of these optical filaments in 3C 58 are  $\sim \pm 900 \text{ km s}^{-1}$  (Fesen, 1983), sufficiently high to indicate that the PWN is young, but too small to account for the current size of 3C 58 if the historical age is assumed – one of several standing problems with regard to its evolution (Chevalier, 2004). A detailed comparison of the X-ray and optical images shows that most of the X-ray filaments do not have corresponding optical structures, however. While comparisons with deeper optical images are clearly needed, the fact that many of the X-ray features without optical counterparts are brighter than average in X-rays suggests that these may actually arise from a different mechanism. Slane et al. (2004) propose that the bulk of the discrete structures seen in the X-ray and radio images of 3C 58 are magnetic loops torn from the toroidal field by kink instabilities. In the inner nebula, the loop sizes are similar to the size of the termination shock radius, as suggested by Begelman (1998). As the structures expand, they enlarge slightly as a consequence of the decreasing pressure in the nebula. Some of the observed X-ray structure in the outermost regions may be the result of thermal filaments produced by Rayleigh-Taylor instabilities, similar to the filaments in the Crab Nebula. A shell of thermal X-ray emission demonstrates the presence of ejecta in these outer regions (Bocchino et al., 2001, Slane et al., 2004a).

It is worth noting that considerable loop-like filamentary structure is evident in *Chandra* observations of the Crab Nebula as well (Weisskopf et al., 2000). These features are primarily observed encircling the bright Crab torus, perpendicular to the toroidal plane, and may result from currents within the torus itself. It is at least conceivable that such currents are signatures of the kink instabilities suggested above.

### 1.3 Large-Scale Structure of PWNe

The large-scale elongated shape of 3C 58 is similar to that found (particularly in the radio band) for a number of other PWNe including the Crab Nebula and G54.1+0.3. Magnetohydrodynamical calculations by Begelman & Li, 1992, and van der Swaluw, 2004, show that such an elongation can result from the pinching effect of a toroidal magnetic field for which the projected axis lies along the long axis of the PWN. The pinching effect results in a low pressure at the edge of the bubble along the major axis with respect to the (higher) pressure at the edge of the minor axis, which yields the elongated structure. The elongation thus marks the projection of the spin axis of the pulsar producing the wound-up field. In 3C 58 this is consistent with the inference of an east-west direction for the projected spin axis based on the interpretation of the extended



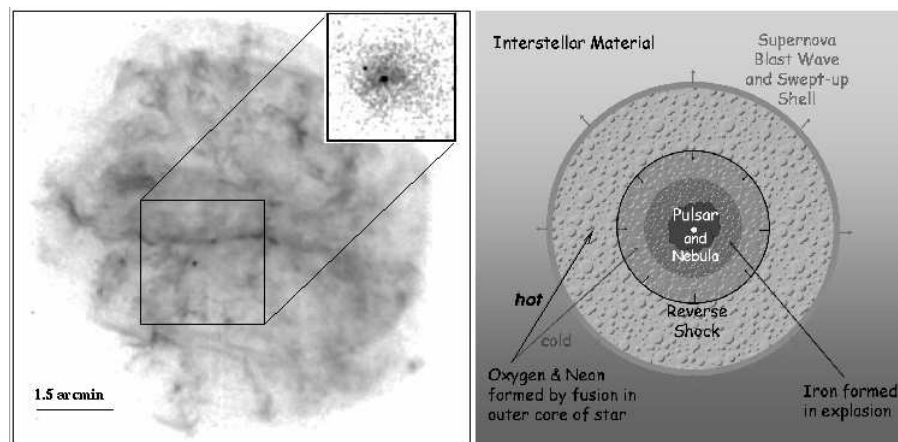


Figure 4. Left: *Chandra* image of G292.0+1.8. The inset shows the central region at energies above 4 keV, where the pulsar and its wind nebula dominate. Right: Schematic diagram of the evolutionary state of G292.0+1.8. The lack of iron observed in the spectrum indicates that the reverse shock has not yet made its way to the center of the remnant, where the PWN resides.

structure in the inner nebula as being associated with a tilted ring-shaped wind termination shock zone (Slane et al., 2002).

The structure of a PWN can be altered significantly through interaction with the reverse shock from the SNR in which it resides. In its early evolution the PWN is basically freely-expanding, encountering only small amounts of slow-moving ejecta in the SNR interior. As the SNR blast wave sweeps up sufficient amounts of circumstellar/interstellar material, a reverse shock is driven back through the ejecta. As this reverse shock propagates, heating the ejecta, it will eventually reach the PWN. *Chandra* studies of the oxygen-rich remnant G292.0+1.8 reveal an SNR in the intermediate stages of this process. The 0.5–10 keV X-ray image is presented in Figure 4 (left), and shows the complex structure associated with the shock-heated ejecta and CSM (Park et al., 2002). The inset shows the central image at energies above 4 keV, and reveals a compact pulsar surrounded by a wind nebula (Hughes et al., 2001, Camilo et al., 2002b, Hughes et al., 2003). X-ray spectra of the SNR show metal-rich ejecta with strong lines of oxygen and neon, but a distinct shortage of iron emission (Park et al., 2004), indicating that the reverse shock has not yet propagated sufficiently far toward the center to heat the iron-rich material that was formed closest to the core of the progenitor (Figure 4, right).

The morphology of the PWNe in G327.1–1.1 presents a rather different picture. The radio image (Figure 5, left) reveals a well-defined SNR shell with a bright PWN in its interior, distinctly offset from the geometric center. A finger of emission extends to the northwest of the radio PWN, and *Chandra*

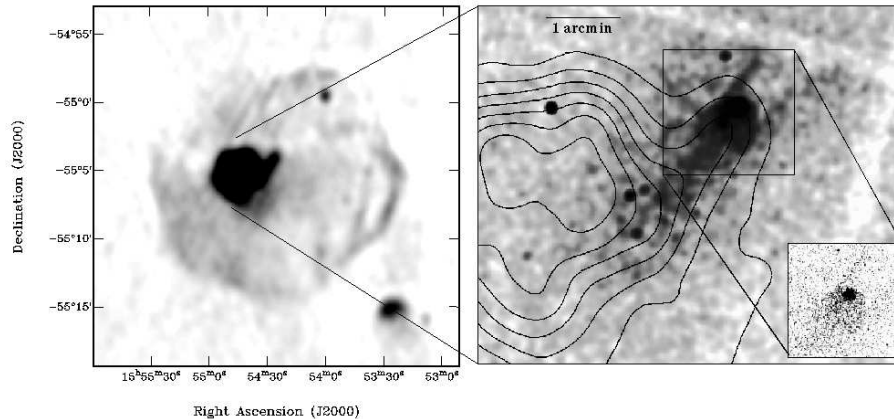


Figure 5. Left: MOST image of the composite SNR G327.1–1.1. Right: *Chandra* image of the PWN in G327.1–1.1 (with radio contours), showing diffuse emission surrounding a compact, but resolved, X-ray source (inset).

observations reveal a compact X-ray source at this location (Figure 5, right). The source is slightly extended (see inset) suggesting that we are seeing material near the wind termination shock. The compact source resides at the tip of a trail of emission that leads back to the bulk of the radio nebula, rather than at the center of the PWN (as in G292.0+1.8, for example), suggesting that the PWN morphology results from a combination of the pulsar motion and the passage of the reverse shock which has apparently disrupted the western side of the nebula (Slane et al., in preparation).

## 2. Neutron Star Cooling

The cooling rate of isolated NSs has been a subject of considerable theoretical work predating even the discovery of the first pulsars (e.g., Bahcall & Wolf 1965). The poorly understood properties of the strong nuclear potential at the densities found in NS interiors make these calculations difficult, and lead to a wide range of predictions based on different assumptions for the equation of state, composition, and details of superconductivity (see, e.g., reviews by Tsutsumi, 1998, and Yakovlev & Pethick, 2004). While there is a clear consensus that the early cooling proceeds via neutrino emission from the NS core, the timescale over which this dominates depends critically on the neutrino production rate which, in turn, can vary by orders of magnitude depending upon the state of matter in the interior.

Broadly speaking, models can be divided into “standard” and “non-standard” cooling scenarios based on the rate of neutrino production in the NS interior. At the high densities and low proton fractions expected in NS interiors, the

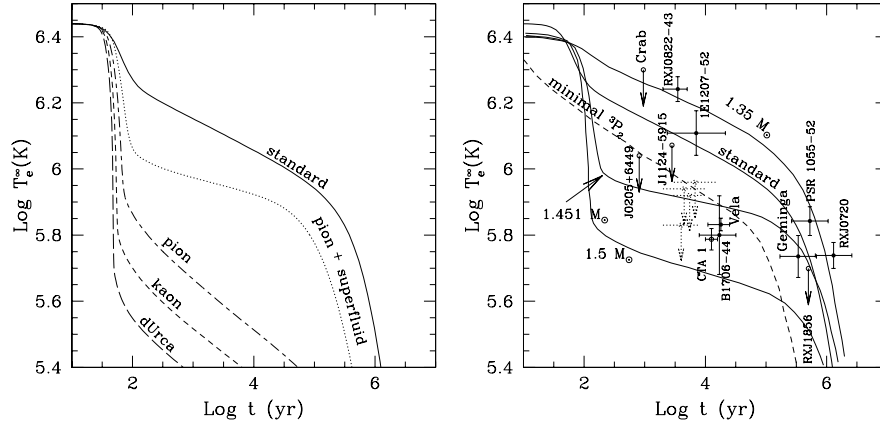


Figure 6. Left: Representative neutron star cooling curves for neutrino rates corresponding to different interior conditions. Data from Page, 1998. Right: Temperature vs. Age measurements for neutron stars, along with plots for standard cooling (bold), “minimal” cooling, and mass-dependent cooling invoking dUrca (see text).

direct Urca reactions ( $n \rightarrow p + e^- + \bar{\nu}_e$  and  $p + e^- \rightarrow n + \nu_e$ ) cannot conserve both energy and momentum. Instead, a bystander baryon is required for each interaction to absorb momentum. The neutrino rate for this so-called modified Urca (mUrca) process is considerably lower than in the direct (dUrca) process because of the extra interaction required, and is the basis for standard cooling models (neutrino bremsstrahlung, and plasmon neutrino processes). In Figure 6 (left), we plot cooling curves for different models of the NS interior and its properties using representative neutrino rates (see Page, 1998 and references therein). The solid curve corresponds to “standard” cooling using an equation of state of moderate stiffness.

Non-standard cooling models incorporate neutrino emissivities associated with other processes that may operate in NS interiors, such as those arising from the presence of pion condensates which may form at sufficiently high densities. The resulting pion-induced beta decay leads to very a high neutrino emissivity and a correspondingly shorter cooling time for the NS interior. Similar processes involving kaon condensates or quark matter may operate as well. Alternatively, equations of state that allow a high proton fraction in the interior may allow the dUrca process to proceed; this also leads to extremely high neutrino production rates (e.g., Kaminker et al., 2002). These nonstandard cooling mechanisms modify the NS cooling curves substantially. The dashed curves in Figure 6 represent approximations for several nonstandard cooling models and illustrate the associated rapid cooling (Page 1998).

The effects of superfluidity can substantially moderate such rapid cooling because the significantly reduced heat capacity of the superfluid particles reduces the neutrino rate considerably. Thus, slow cooling can occur from a com-

bination of slow neutrino rates and a high degree of superfluidity, while rapid cooling places strong constraints on both, and thus on the structure and physics of the NS interior, as well as on the microphysics of superfluidity. In particular, as the temperature approaches the critical temperature for the superfluid state, the formation and breaking of Cooper pairs opens another channel for neutrino emission that can lead to more rapid cooling. Page et al., 2004 have calculated a “minimal cooling” scenario which extends the standard mUrca cooling scenario to include the contributions from this Cooper pair process. As discussed below, for some superfluidity models they find sufficiently rapid cooling to explain most observations of young NSs. Yakovlev and Pethick, 2004, on the other hand, have considered both standard and enhanced cooling models. Using the NS mass as a free parameter, they find models for which the dUrca process becomes active for sufficiently high masses, thus leading to a picture in which the young, cool NSs correspond to those with higher mass (see below).

## 2.1 Measuring Neutron Star Temperatures

Treating the emission from the NS surface as a blackbody, X-ray spectral fitting provides a measure of the gravitationally redshifted temperature and luminosity (assuming the distance is known):

$$T_s^\infty = \left[ 1 - \sqrt{\frac{2GM}{Rc^2}} \right] T_s; L^\infty = \left[ 1 - \sqrt{\frac{2GM}{Rc^2}} \right]^2 L \quad (2)$$

where the quantities on the left are observed at infinity, and those on the right are at the NS surface;  $M$  and  $R$  are the mass and radius of the NS. From this we calculate the effective radius, which can be compared directly with predications for different equations of state:  $R_{eff}^2 = L^\infty / [4\pi\sigma(T_s^\infty)^4]$  (where  $\sigma$  is the Stefan-Boltzmann constant). Alternatively, if only an upper limit on the source luminosity is determined, a temperature upper limit can be derived by assuming a value for the NS radius.

As with all stars, the emission from the surface of a NS is not a blackbody; rather, it is modified by the presence of whatever atmosphere might exist. One expects the surface of the NS to be covered with Fe, but an atmosphere consisting of H, He, and/or intermediate-mass elements acquired either from ejecta fallback following the neutron star’s formation, or from material accreted from the ISM, is also a possibility. From models of nonmagnetic atmospheres, the primary effect of H or He atmospheres is a considerable deviation of the high energy end of the spectrum relative to the Wien tail of a pure blackbody. The result is that attempts to fit the observed emission with a blackbody model will overestimate the effective temperature – typically by as much as a factor of two. The inferred size of the NS would, in turn, be underestimated in order to

yield the same flux. For atmospheres dominated by heavier elements the effect is considerably reduced, and the blackbody fit gives a good approximation to the temperature.

## 2.2 Confronting Cooling Models

In Figure 6 (right) we plot the measured temperatures, or upper limits, for the pulsars and compact objects in SNRs for which these values are best determined. Values for known pulsars are plotted with closed circles. For comparison, curves are shown for standard cooling as well as the “minimal” cooling model of Page et al., 2004 (dashed curve). The latter model assumes no enhanced cooling mechanisms in the interior. The primary mechanism which results in faster cooling is neutrino emission from the Cooper pair breaking and formation process, which is heavily dependent upon the assumed superfluidity model (here we have plotted their model “a” for the neutron  ${}^3\text{P}_2$  gap); the predicted cooling rate is sufficiently rapid to explain the measurements for most pulsars, although the temperatures for the Vela Pulsar and J0205+6449 in 3C 58 fall appear to require more rapid cooling. The inferred temperature for RX J0007.0+7302 (plotted as an open box in Figure 6), a compact X-ray source in the SNR CTA 1, also falls below this minimal cooling scenario (Slane et al., 2004). While pulsations have yet to be detected from this source, *Chandra* observations by Halpern et al., 2004 reveal a slightly extended source with a distinct jet-like tail that is the signature of the pulsar outflows described in Section 1.2.

For comparison, cooling curves illustrating the effects of increasing mass are plotted as solid curves, using the model 1p for proton superfluidity from Yakovlev and Pethick, 2004. Also plotted in the Figure, as dashed arrows, are upper limits based on a neutron star search in nearby SNRs (Kaplan et al., 2004). In this study, deep X-ray observations were used to identify, sources within the field of the SNRs, and follow-up optical and IR observations were used to screen for non-NS counterparts. While the lack of detection of a NS in these remnants (G127.1+0.5, G84.2-0.8, G93.3+6.9, and G315.4-2.3 in increasing order of temperature upper limit) may indicate that these SNRs originated in Type Ia events, or all formed black holes, this is statistically unlikely. Future measurements from this study will solidify this picture, and perhaps provide further evidence for rapid cooling in young neutron stars.

## 3. Summary

Due in large part to the availability of high resolution X-ray measurements, the study of young NSs and their PWNe have yielded dramatic new information on the nature of the stellar interiors and the structure of their winds. It is now clear that the axisymmetric wind from a pulsar goes through a termi-

nation shock as it joins the slower flow of its extended nebula, and that jets and toroidal structures characterizing the inner structure can be used to infer the orientation of the pulsar spin axis. The brightness variations in the inner nebula and jets, as well as the spectral and spatial structure of these regions, yield information on the outflow geometry as well as the fraction of spin-down energy being channeled into these regions. With broad application to particle acceleration and jet formation in astrophysical settings, these observations are providing constraints on theoretical models of considerable importance for a wide range of problems. Similarly, new observations are providing unprecedented capabilities for detecting young neutron stars in SNRs, and for characterizing their emission. These have forced a revised look at models for the structure of NS interiors and provide the best opportunity for addressing the possibility that exotic states of matter reside in NS cores. Through additional and more sensitive observations of these systems, we anticipate significant refinements, and undoubtedly new surprises, in broad picture of their structure that is currently unfolding.

### **Acknowledgments**

The author wish to thank Bryan Gaensler, David Helfand, Jack Hughes, and Fred Seward for their particular contributions to this work. Informative discussions on NS cooling with Dima Yakovlev and Dany Page are also gratefully acknowledged. This work was supported in part by NASA contract NAS8-39073 and grants GO0-1117A, NAG5-9281, and GO1-2054X.

## References

- Aschenbach, B. and Brinkmann, W. (1975). A model of the x-ray structure of the Crab Nebula. *A&A*, 41:147.
- Bahcall, J. N. and Wolf, R. A. (1965). An Observational Test of Theories of Neutron-Star Cooling. *ApJ*, 142:1254–1256.
- Begelman, M. C. (1998). Instability of Toroidal Magnetic Field in Jets and Plerions. *ApJ*, 493:291.
- Begelman, M. C. and Li, Z. (1992). An axisymmetric magnetohydrodynamic model for the Crab pulsar wind bubble. *ApJ*, 397:187–195.
- Bocchino, F., Warwick, R. S., Marty, P., Lumb, D., Becker, W., and Pigot, C. (2001). The x-ray nebula of the filled center supernova remnant 3C 58 and its interaction with the environment. *A&A*, 369:1078–1087.
- Bucciantini, N., Amato, E., Bandiera, R., Blondin, J. M., and Del Zanna, L. (2004). Magnetic Rayleigh-Taylor instability for Pulsar Wind Nebulae in expanding Supernova Remnants. *A&A*, 423:253–265.
- Camilo, F., Lorimer, D. R., Bhat, N. D. R., Gotthelf, E. V., Halpern, J. P., Wang, Q. D., Lu, F. J., and Mirabal, N. (2002a). Discovery of a 136 millisecond radio and x-ray pulsar in supernova remnant G54.1+0.3. *ApJ*, 574:L71–L74.
- Camilo, F., Manchester, R. N., Gaensler, B. M., Lorimer, D. L., and Sarkissian, J. (2002b). PSR J1124–5916: A young and energetic pulsar in supernova remnant G292.0+1.8. *ApJ*, 567:L71–L75.
- Chevalier, R. A. (2004). Pulsar wind nebulae: theoretical aspects and observational constraints. *Advances in Space Research*, 33:456–460.
- Fesen, R. A. (1983). Discovery of large radial velocities in the supernova remnant 3C 58. *ApJL*, 270:L53–L57.
- Frail, D. A. and Moffett, D. A. (1993). Deep VLA imaging of pulsar-powered nebulae and the beaming fraction of young pulsars. *ApJ*, 408:637–645.
- Gaensler, B. M., Arons, J., Kaspi, V. M., Pivovarov, M. J., Kawai, N., and Tamura, K. (2002). High-resolution X-ray imaging of pulsar B1509–58 and its environment. *ApJ*, 569:878–893.
- Gallant, Y. A. and Arons, J. (1994). Structure of relativistic shocks in pulsar winds: A model of the wisps in the Crab Nebula. *ApJ*, 435:230.
- Halpern, J. P., Gotthelf, E. V., Camilo, F., Helfand, D. J., and Ransom, S. M. (2004). X-Ray, Radio, and Optical Observations of the Putative Pulsar in the Supernova Remnant CTA 1. *ApJ*, 612:398–407.
- Helfand, D. J., Gotthelf, E. V., and Halpern, J. P. (2001). Vela Pulsar and Its Synchrotron Nebula. *ApJ*, 556:380–391.
- Hester, J. J. (1998). Wind interactions in the Crab Nebula. *Mem. della Soc. Ast. It.*, 69:883.
- Hester, J. J., Mori, K., Burrows, D., Gallagher, J. S., Graham, J. R., Halverson, M., Kader, A., Michel, F. C., and Scowen, P. (2002). Hubble Space Telescope and Chandra Monitoring of the Crab Synchrotron Nebula. *ApJL*, 577:L49–L52.
- Hester, J. J., Stone, J. M., Scowen, P. A., Jun, B., Gallagher, J. S., Norman, M. L., Ballester, G. E., Burrows, C. J., Casertano, S., Clarke, J. T., Crisp, D., Griffiths, R. E., Hoessel, J. G., Holtzman, J. A., Krist, J., Mould, J. R., Sankrit, R., Stapelfeldt, K. R., Trauger, J. T., Watson, A., and Westphal, J. A. (1996). WFPC2 Studies of the Crab Nebula. III. Magnetic Rayleigh-Taylor Instabilities and the Origin of the Filaments. *ApJ*, 456:225–233.

- Hughes, J. P., Slane, P. O., Burrows, D. N., Garmire, G., Nousek, J. A., Olbert, C. M., and Keohane, J. W. (2001). A pulsar wind nebula in the oxygen-rich supernova remnant G292.0+1.8. *ApJ*, 559:L153–L156.
- Hughes, J. P., Slane, P. O., Park, S., Roming, P. W. A., and Burrows, D. N. (2003). An x-ray pulsar in the oxygen-rich supernova remnant G292.0+1.8. *ApJ*, 591:L139–L142.
- Jun, B. (1998). Interaction of a Pulsar Wind with the Expanding Supernova Remnant. *ApJ*, 499:282.
- Kaminker, A. D., Yakovlev, D. G., and Gnedin, O. Y. (2002). Three types of cooling superfluid neutron stars: Theory and observations. *A&A*, 383:1076–1087.
- Kaplan, D. L., Frail, D. A., Gaensler, B. M., Gotthelf, E. V., Kulkarni, S. R., Slane, P. O., and Nechita, A. (2004). An X-Ray Search for Compact Central Sources in Supernova Remnants. I. SNRS G093.3+6.9, G315.4-2.3, G084.2+0.8, and G127.1+0.5. *ApJS*, 153:269–315.
- Kaspi, V. M., Roberts, M. S. E., and Harding, A. K. (2004). Isolated neutron stars. In Lewin, W. H. G. and van der Klis, M., editors, *Compact Stellar X-ray Sources*, Cambridge. CUP. in press (astro-ph/0402136).
- Kaspi, V. M., Roberts, M. S. E., Vasisht, G., Gotthelf, E. V., Pivovarov, M., and Kawai, N. (2001). Chandra observations of G11.2-0.3: Implications for pulsar ages. *ApJ*, 560:371–377.
- Kennel, C. F. and Coroniti, F. V. (1984). Magnetohydrodynamic model of Crab Nebula radiation. *ApJ*, 283:710–730.
- Komissarov, S. S. and Lyubarsky, Y. E. (2004). Synchrotron nebulae created by anisotropic magnetized pulsar winds. *MNRAS*, 349:779–792.
- Lai, D., Chernoff, D. F., and Cordes, J. M. (2001). Pulsar jets: implications for neutron star kicks and initial spins. *ApJ*, 549:1111–1118.
- Lu, F. J., Wang, Q. D., Aschenbach, B., Durouchoux, P., and Song, L. M. (2002). Chandra observation of supernova remnant G54.1+0.3: A close cousin of the Crab Nebula. *ApJ*, 568:L49–L52.
- Murray, S. S., Slane, P. O., Seward, F. D., Ransom, S. M., and Gaensler, B. M. (2002). Discovery of x-ray pulsations from the compact central source in the supernova remnant 3C 58. *ApJ*, 568:226–231.
- Ng, C.-Y. and Romani, R. W. (2004). Fitting pulsar wind tori. *ApJ*, 601:479–484.
- Page, D. (1998). Thermal evolution of isolated neutron stars. In *The Many Faces of Neutron Stars*. Edited by R. Buccheri, J. van Paradijs, and M. A. Alpar. Dordrecht ; Boston : Kluwer Academic Publishers, 1998., p.539, pages 539.
- Page, D., Lattimer, J. M., Prakash, M., and Steiner, A. W. (2004). Minimal Cooling of Neutron Stars: A New Paradigm. in press (astro-ph/0403657).
- Park, S., Hughes, J. P., Slane, P. O., Burrows, D. N., Roming, P. W. A., Nousek, J. A., and Garmire, G. P. (2004). Nucleosynthesis in the Oxygen-rich Supernova Remnant G292.0+1.8 from Chandra X-Ray Spectroscopy. *ApJ*, 602:L33–L36.
- Park, S., Roming, P. W. A., Hughes, J. P., Slane, P. O., Burrows, D. N., Garmire, G. P., and Nousek, J. A. (2002). The structure of the oxygen-rich supernova remnant G292.0+1.8 from Chandra x-ray images: shocked ejecta and circumstellar medium. *ApJ*, 564:L39–L44.
- Pavlov, G. G., Teter, M. A., Kargaltsev, O., and Sanwal, D. (2003). The Variable Jet of the Vela Pulsar. *ApJ*, 591:1157–1171.
- Rees, M. J. and Gunn, J. E. (1974). The origin of the magnetic field and relativistic particles in the Crab Nebula. *MNRAS*, 167:1–12.
- Reynolds, S. P. (1988). Filamentary structure in Crab-like supernova remnants. *ApJ*, 327:853–858.



- Reynolds, S. P. and Aller, H. D. (1988). Radio observations of the Crab-like supernova remnant 3C 58. I - Total intensity observations. *ApJ*, 327:845–852.
- Romani, R. W. and Ng, C.-Y. (2003). The Pulsar Wind Nebula Torus of PSR J0538+2817 and the Origin of Pulsar Velocities. *ApJL*, 585:L41–L44.
- Slane, P., Helfand, D. J., van der Swaluw, E., and Murray, S. S. (2004a). New constraints on the structure and evolution of the pulsar wind nebula 3C 58. *ApJ*. in press (astro-ph/0405380).
- Slane, P., Zimmerman, E. R., Hughes, J. P., Seward, F. D., Gaensler, B. M., and Clarke, M. J. (2004b). X-Ray Observations of the Compact Source in CTA 1. *ApJ*, 601:1045–1049.
- Slane, P. O., Helfand, D. J., and Murray, S. S. (2002). New constraints on neutron star cooling from Chandra observations of 3C 58. *ApJ*, 571:L45–L49.
- Tsuruta, S. (1998). Thermal properties and detectability of neutron stars. II. Thermal evolution of rotation-powered neutron stars. *Phys Rep*, 292:1–130.
- van den Bergh, S. (1978). Observations of the Optical Remnant of SN 1181 = 3C 58. *ApJL*, 220:L9.
- van der Swaluw, E., Downes, T. P., and Keegan, R. (2004). An evolutionary model for pulsar-driven supernova remnants. A hydrodynamical model. *A&A*, 420:937–944.
- Weisskopf, M. C., Hester, J. J., Tennant, A. F., Elsner, R. F., Schulz, N. S., Marshall, H. L., Karovska, M., Nichols, J. S., Swartz, D. A., Kolodziejczak, J. J., and O’Dell, S. L. (2000). Discovery of spatial and spectral structure in the x-ray emission from the Crab Nebula. *ApJ*, 536:L81–L84.
- Yakovlev, D. G. and Pethick, C. J. (2004). Neutron Star Cooling. *Ann. Rev. Astr. Ap.*, 42:169–210.